

T.-J. Zhou · Z.-X. Li

Simulation of the east asian summer monsoon using a variable resolution atmospheric GCM

Received: 9 January 2001 / Accepted: 30 October 2001 / Published online: 27 February 2002
© Springer-Verlag 2002

Abstract The East Asia summer monsoon (EASM) is simulated with a variable resolution global atmospheric general circulation model (GCM) developed at the Laboratoire de Météorologie Dynamique, France. The version used has a local zoom centered on China. This study validates the model's capability in reproducing the fundamental features of the EASM. The monsoon behaviors over East Asia revealed by the ECMWF reanalysis data are also addressed systematically, providing as observational evidence. The mean state of the EASM is generally portrayed well in the model, including the large-scale monsoon airflows, the monsoonal meridional circulation, the cross-equatorial low-level jets, the monsoon trough in the South China Sea, the surface cold high in Australia, and the upper-level northeasterly return flow. While the performance of simulating large-scale monsoonal climate is encouraging, the model's main deficiency lies in the rainfall. The marked rainbelt observed along the Yangtze River Valley is missed in the simulation. This is due to the weakly reproduced monsoonal components in essence and is directly related to the weak western Pacific subtropical high, which leads to a fragile subtropical southwest monsoon on its western flank and results in a weaker convergence of the southwest monsoon flow with the midlatitude westerlies. The excessively westward extension of the high, together with the distorted Indian low, also makes the contribution of the tropical

southwest monsoon to the moisture convergence over the Yangtze River Valley too weak in the model. The insufficient plateau heating and the resulting weak land-sea thermal contrast are responsible for the weakly reproduced monsoon. It is the deficiency of the model in handling the low-level cloud cover over the plateau rather than the horizontal resolution and the associated depiction of plateau topography that results in the insufficient plateau heating. Comparison with the simulation employing regular coarser mesh model reveals that the local zoom technique improves, in a general manner, the EASM simulation.

1 Introduction

Due to its particular geographical location, South and East Asia experiences the largest monsoonal climate anywhere on the Earth. The summer monsoon especially has a large impact on the social and economic activities of the region. Traditionally, two sub-systems can be distinguished: the Indian summer monsoon and the East Asian summer monsoon (hereafter referred to as EASM). In the past, the Indian summer monsoon has received a great attention from the climate research community. See, e.g., Krishnamurti and Bhalme (1976), Webster and Yang (1992), Latif et al. (1994), Webster et al. (1998), Vernekar and Ji (1999), among others. The EASM however has been studied much less. Much progress has been made in recent years, thanks to satellite observations, field experiments and numerical simulations (Zeng et al. 1988; Shukla et al. 1992; Sperber et al. 1994; Samel and Wang et al. 1995; Lau and Yang 1996; Li and Yanai 1996; Liang and Wang 1998). There are many resemblances between the two monsoons. Both of them have cross-equator flow, monsoon troughs and intense precipitations. They are also related to each other by their geographical approximation. However, the EASM cannot be regarded as a simple eastward extension of the Indian summer

T.-J. Zhou · Z.-X. Li (✉)
Laboratoire de Météorologie Dynamique/CNRS,
case courrier 99, Université Paris 6,
4 Place Jussieu, 75252 Paris cedex 05, France
E-mail: li@lmd.jussieu.fr
E-mail: zhoutj@lasg.iap.ac.cn

T.-J. Zhou
Also at National Key Laboratory of Numerical Modelling for
Atmospheric Sciences and Geophysical Fluid Dynamics (LASG),
Institute of Atmospheric Physics, Chinese Academy of Sciences,
Mail Box 9804, 100029 Beijing, China

monsoon, since it has its own circulation patterns and independent climate behavior. In fact, the Indian summer monsoon is mainly a tropical monsoon, the EASM is however composed of both tropical and subtropical components (see the reviews of Tao and Chen 1987; Chen et al. 1991; Ding 1994).

Currently, quantitative studies of the monsoon system are mainly based on numerical experiments of atmospheric general circulation models (GCMs). Due to the presence of complex topography and insufficient model resolution in the region, current GCMs often have a very mediocre performance in simulating the EASM (Liang and Wang 1998; Yu et al. 2000). Regional models may have a better resolution in the monsoon region. They have given very successful results (e.g., Liu et al. 1994, 1996; Wang et al. 2000; Gong and Wang 2000), showing the importance of good representation of the local topography. Regional models are, however, dependent upon the boundary zone prescription, which limits their utility in studying long-term climate behaviors.

Using variable resolution in a global GCM is an interesting approach in regional climate studies. The Laboratoire de Météorologie Dynamique (LMD) model has been successfully used in such a configuration to study the climate of Antarctica (Krinner et al. 1997) and South America (Menendez et al. 2001). Deque and Piedelievre (1995) have also shown utility of such an approach over Europe in the GCM of Meteo-France. Here we use a high-resolution version of the LMD model with a local zoom centered on China. The main purpose is to evaluate its performance in reproducing the EASM. At the same time, the complex topography of the region also provides a good test-bed for checking the behavior of the zoom.

The other sections are organized as follows. The LMD model used in the present study is described in Sect. 2. The simulated EASM, together with a discussion on the typical features of the EASM system revealed by observational data, are presented in Sect. 3. The effects of local zoom, together with an inspection on the physical processes responsible for the model's performance in reproducing the EASM, are discussed in Sect. 4. Highlights of the findings are summarized in Sect. 5.

2 Model description and experimental design

The LMD GCM is a state-of-the-art climate model and has been widely used in Indian summer monsoon studies (Laval et al. 1996; Sharma et al. 1998). Its capability in reproducing the EASM has, however, never been evaluated. The model used is the LMDZ, version 3.2. It is derived from the standard version described in Sadourny and Laval (1984). The model is formulated in the finite-difference grid with 120 points in longitude, 91 points in latitude and 19 hybrid vertical layers. The center of the zoom is currently at 119°E/30°N where the resolution is 1° in latitude by 1.5° in longitude. Figure 1 shows the model grid and topography in the region of South and East Asia. The complex terrain of the region is very well represented in the model.

A brief description of the physical parametrization and the model's main performance in simulating interannual climate

variability are presented in Li (1999). The model has evolved in the following ways. The convection scheme is that developed by Tiedtke (1989). It is a simple mass-flux scheme. The closures (both triggering conditions and entrainment/detrainment rates) are based on the surface evaporation and large-scale water-vapor convergence. The cloud parametrization is a prognostic scheme, as described in Le Treut and Li (1991). At present, only clouds associated with stratiform precipitation are taken into account. Those created by convection are diagnosed following the intensity of convective precipitation (Slingo 1987). For the radiative transfer, the diurnal cycle is now explicitly calculated, however, Li (1999) calculated only the daily mean. The surface model is a bucket model for which we consider a homogeneous layer of 150 mm. The calculation of the surface temperature is incorporated in the boundary layer and based on the surface energy balance equation. For the surface moisture, a holding capacity is fixed at 150 mm of water, and all the water above this value is lost as runoff.

The model was run in a climatological mode. The distributions of sea-surface temperature and sea ice are climatological ones, obtained from observations for the period 1979–1993. Monthly values at the initial grid of 2.5° were first interpolated into daily values and into the model grid. A simulation of 11 years was run and the last 10 years are used for comparison with observations.

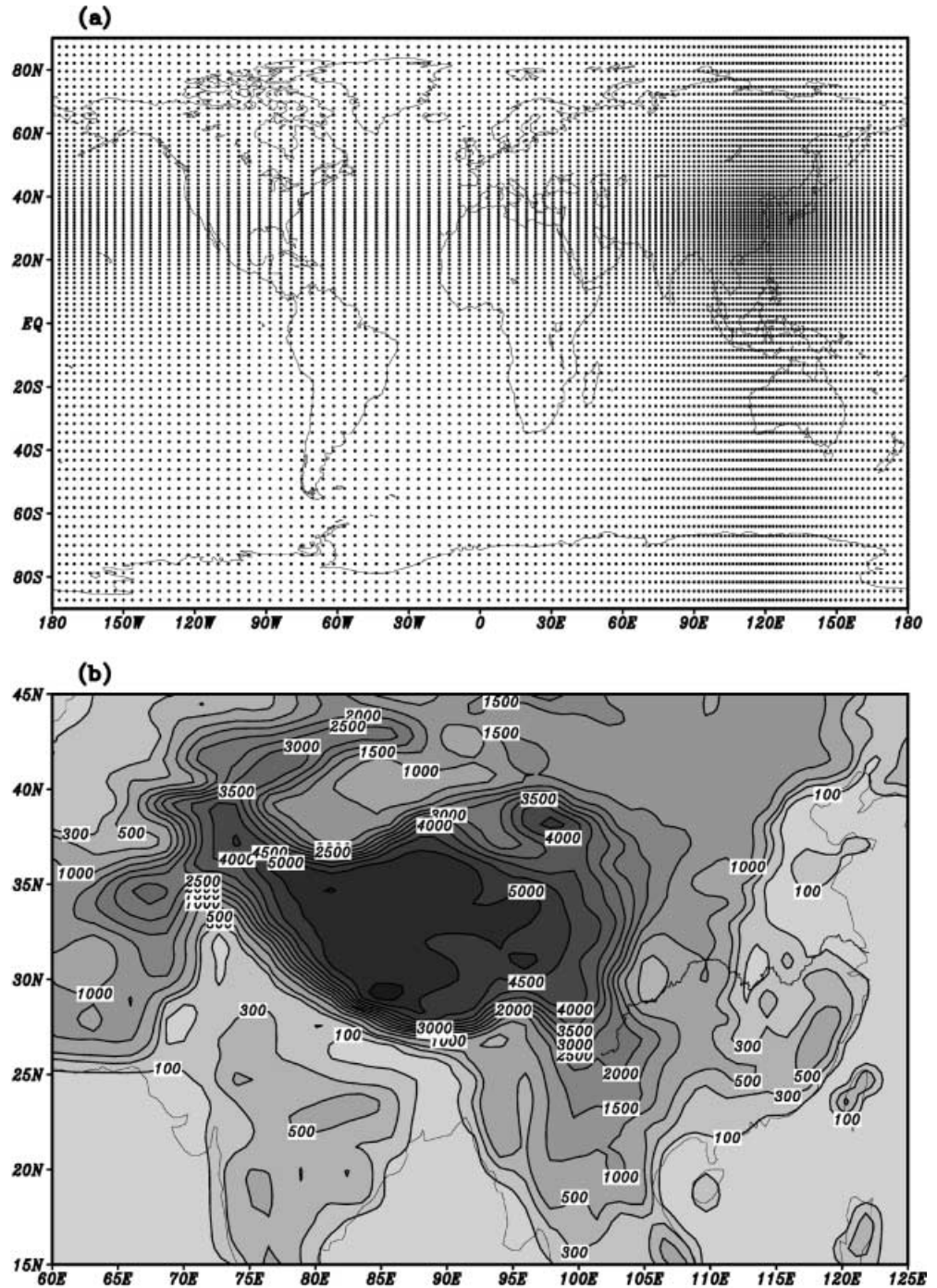
Two major observational datasets are used in the present study. The first one is the ERA-15 dataset (ECMWF re-analysis for the period 1979–93, see Gibson et al. 1997). It contains the main meteorological variables, such as temperature, humidity and winds in three dimensions. The second one is the climatological precipitations compiled by Xie and Arkin (1997). It covers 1979–98. It is obtained from gauge observations, satellite estimations and numerical model outputs. Comparison (Yu et al. 2000) with 106 meteorological stations of East China (data provided by the Chinese Meteorological Administration) shows that the Xie and Arkin (1997) precipitation data are reliable in this region and can be used to validate climate models. For convenient reasons, all datasets and model outputs are interpolated into a common grid of 2.5°×2.5° before comparison. This study presents only the mean state of the June–July–August (JJA) period, the seasonal migration being presented in a separate work.

3 Results

As summarized by Krishnamurti and Bhalme (1976), the Indian summer monsoon is not limited to the heavy rainfall and large cloud cover over the Indian Peninsula. It is also characterized by particular circulation patterns. In the lower layer of the atmosphere, the trade wind from the Mascarene high crosses the equator off the East African coast and turns to northeast. This Somali jet crosses the Arabian Sea and the Bay of Bengal, and forms the monsoon trough over North India. In the upper layer, an intense tropical easterly jet stream is associated with the anticyclone over the Tibetan Plateau.

Cross-equator flows also exist outside the East African coast. Observations reveal that there are four other flows located at 85°E, 105°E, 130°E and 150°E, respectively. They are related to the surface cold high pressure zone over Australia and the associated trade wind in the Southern Hemisphere. They form the main monsoon flows for East Asia in summer. A monsoon trough can also be traced in the South China Sea and western Pacific. This corresponds to the intertropical convergence zone (ITCZ) where intense precipitation is observed. When all these monsoonal flows (including the

Fig. 1. **a** Schematic representation of the global model grid with zoom at 119°E/30°N. **b** Model topography (m) for the region of South and East Asia



Indian summer monsoon flow) reach the northern part of the South China Sea and in the northwest Pacific, they can be accelerated by the subtropical anticyclone over the northwest Pacific and directed further north, to reach the relatively high latitudes of East Asia. In the western and northern flanks of the subtropical anticyclone, a frontal zone is often formed and intense precipitations (Meiyu or Plum rain system) are observed and move meridionally when the front moves. Given the subtropical character of the EASM, mid-latitude disturbances can also play important roles in determining the frontal precipitation.

In the forthcoming analysis, we will examine first the horizontal circulation patterns in Southeast Asia and then the meridional circulation and the cross-equator jets.

3.1 Horizontal circulation patterns

Figure 2 plots the JJA mean stream lines of 850 hPa for ERA and LMD, respectively. At the 850 hPa level, both Mascarene and Australian anticyclones in the Southern Hemisphere are correctly simulated. To the north of

these two anticyclones, there exist strong southeast trade winds which cross the equator in the Indian Ocean, South China Sea and western Pacific. After crossing the equator, they become monsoon flows and blow to the east and north. For both observation and simulation, monsoon troughs can be observed in the Bay of Bengal and South China Sea. The subtropical high over the western Pacific extends too far westwards. This explains why the monsoon flow limit (where the monsoonal airflow meets the trade wind and then deflects northwards) is over the Philippines and Taiwan island in the model and to the east of Philippines in the observation.

At the level of 500 hPa (Fig. 3), the Iranian high and the western Pacific high dominate the subtropical latitudes of the Northern Hemisphere. Note in observation, a shear line occurs over the Yangtze River Valley. North of the shear line, cold anticyclonic air moves eastwards to the ocean, while in the south, warm and moist southwest monsoon flow, coming from the western Pacific, Indo-China Peninsula, and South China Sea, reaches the Yangtze River Valley along the shear line. The midlatitude cold air converges with the southwesterly warm air over the Yangtze River Valley, resulting in the Meiyu front and abundant rainfall. The lower

tropospheric convergence over there will be discussed in the forthcoming analysis of the meridional circulation. Notice that the contribution of the Indian monsoonal circulation to the convergence over Yangtze River Valley is not obvious in the simulation. The reason is that the simulated low pressure over the Indian Peninsula shifts to the Arabian Sea and the westerly airflow deflects to the north over the Bay of Bengal rather than over the South China Sea. This is again coherent with the circulation at 850 hPa, showing a systematical model discrepancy: the westward shift of the subtropical anticyclone in the lower atmosphere.

Figure 4 shows the summertime 500-hPa temperature field for the observation and the simulation. The most significant feature is the warm center situated over the Tibetan Plateau (30°N/90°E). The simulated warm center shifts southwards and locates over the northeastern corner of the Indian subcontinent. For the condition over the Tibetan Plateau, the model center is too weak (about 3 °C colder). This discrepancy, also detectable at other adjacent levels including the surface, is related to the insufficient plateau heating, which will be addressed in detail in the following discussion section. Over the tropical Indian Ocean, however, the model is warmer than the observation. This ‘cold-north-warm-south’ structure indicates a weakly reproduced land-sea

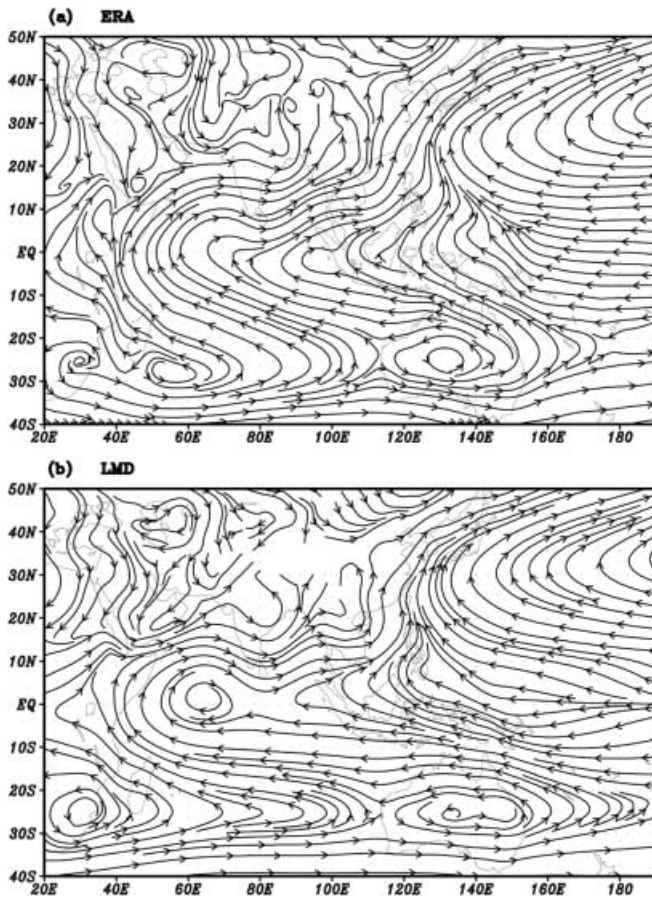


Fig. 2. 850-hPa stream line for the period of June–July–August (JJA), from the ECMWF reanalysis (a, ERA) and the model (b, LMD) respectively

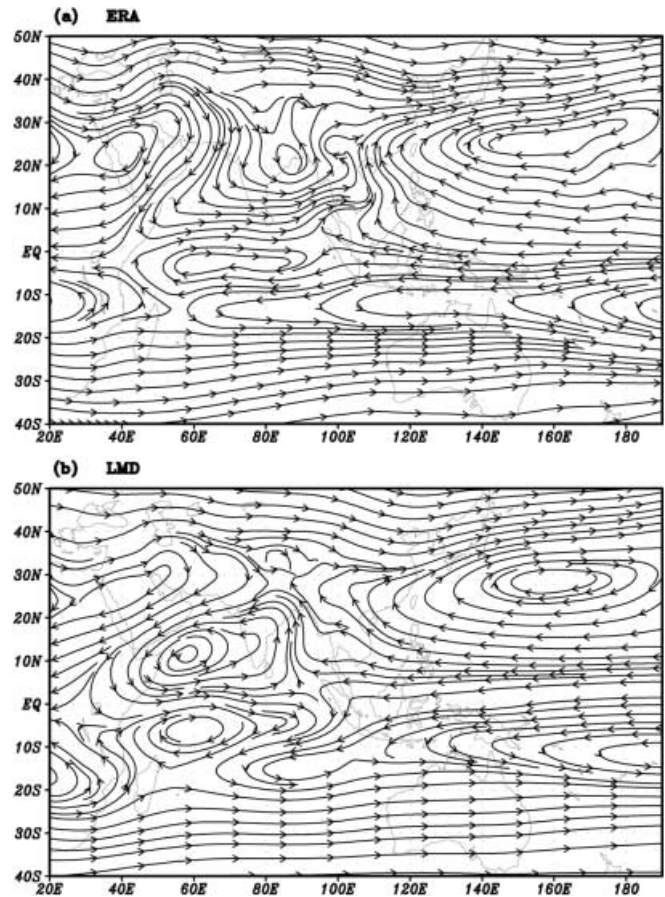


Fig. 3a, b. Same as in Fig. 2, but for 500 hPa

thermal contrast, and is a main factor for the insufficient northward movement of the monsoon precipitations which will be shown later.

The JJA mean 500-hPa geopotential height is shown in Fig. 5 for both the observation and simulation. The position of the ridge line for the subtropical high over the northwest Pacific is correctly simulated in latitude. The subtropical high extends too far westwards in the model, but its intensity is too weak in comparison with the observation. For the observation, the 5870 geopotential meter (gpm) line reaches Taiwan in the west, and a large region over the northwestern Pacific is dominated by isolines greater than 5880-gpm. In the model, however, only the 5860-gpm line reaches Taiwan at the western end, and the isoline of 5870-gpm retreats eastwards. The 5880-gpm line is almost absent in the simulation. In addition, the observed low pressure trough over the Indian subcontinent is not strong enough in the simulation. This is coherent with the 500-hPa streamlines.

Figure 6 shows the JJA mean streamlines at 200 hPa. A huge anticyclone dominates the tropical African–Asian region to the south of 40°N. The huge anticyclonic circulation consists of a westerly jet about 5°–8° north of the Yangtze River Valley, and a northeasterly flow south of the Meiyu front. Thus, a northeasterly flow prevails over East Asia, forming a prominent

return flow lying over the low-level southwesterly and southerly monsoonal flows depicted in Figs. 2 and 3. The anticyclone also provides a favorable divergent field for the underlying convective activity along the Meiyu front. To the south of the huge anticyclone, an upper-level easterly jet exists, and it has two branches: one over the southern tip of the Indian Peninsula, and the other over the southern part of the South China Sea. The simulated second branch shifts southeastwards to some extent. Notice also the meridional component of the northeasterly flow in the simulation is weaker than that in the ERA data, indicating a weaker return flow.

One important aspect of planetary scale circulation for monsoon is the divergent circulation at 200 hPa, usually displayed by the velocity potential. As shown in Fig. 7a, the region with the strongest divergent wind is found over the Philippines and its adjacent sea area. The divergent outflow encompasses the regions of the Indian monsoon and the EASM. The divergent wind flows southwards from the center to Australia and the southern Indian Ocean, to the convergent center over the Mozambique Channel. It also flows eastwards to the mid-Pacific, and westwards to the Iranian high. The maxima of the divergent winds are located over China and the region from the Bay of Bengal to Indonesia. As shown in Fig. 7b, the model is qualita-

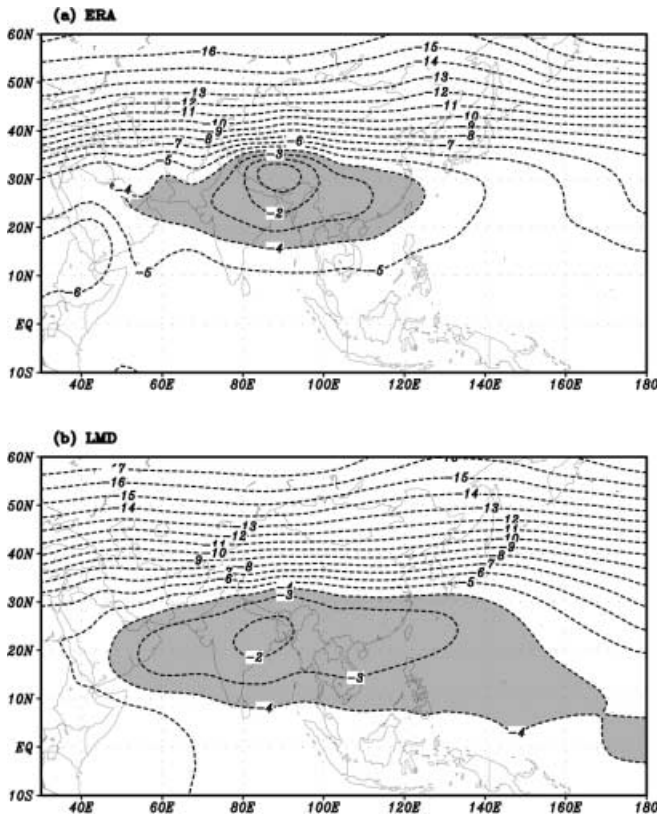


Fig. 4. JJA mean temperature at 500 hPa for the ECMWF reanalysis (a, ERA); and the model (b, LMD) respectively. Contour interval is 2 °C. Shaded are regions warmer than -4 °C

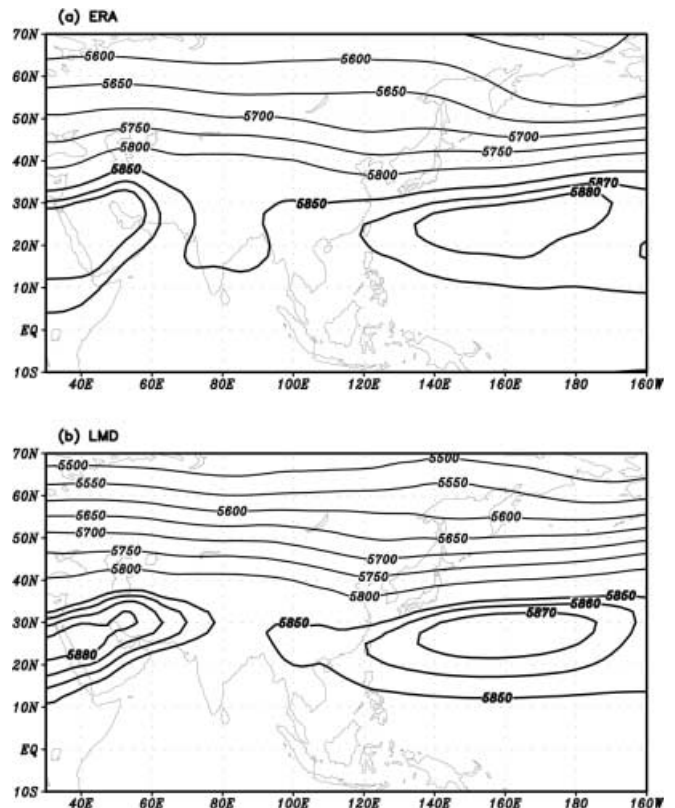


Fig. 5. JJA mean geopotential height (gpm) at 500 hPa for the ECMWF reanalysis (a, ERA) and the model (b, LMD) respectively. Contour interval is 50 gpm. The isolines of 5850, 5870 and 5880 are highlighted

tively consistent with the observation in the positions of divergent and convergent centers. The simulation is, however, much weaker than the observation. For instance, the intensity of the divergent center over the Philippines and the South China Sea is about 30% weaker in the model than in the observation. The weaker upper level divergence also indicates a weakly reproduced monsoon.

3.2 Cross-equator low-level jets and monsoonal meridional cell

Cross-equator low-level jets are typical for monsoon circulation. The Somali jet originates from the East African coast. This strong low-level westerly flow, from the Arabian Sea to southwest China, can exert influences on the EASM. But its influence is recognized to be marginal for the rainfall in East Asia (Wang and Leftwich 1984). Other cross-equator low-level jets in the South China Sea and the western Pacific have larger importance. Li (1956) has already reported the influence of the Australian anticyclone in the development of synoptic systems in China.

Figure 8 displays a cross section of the JJA mean meridional wind along the equator for ERA and LMD

respectively. Five cross-equatorial jets can be observed. The most vigorous is the Somali jet situated at 42°E and 900 hPa. To the east, over the Malaysian-Borneo region (80°–85°E), a low-level jet can be observed, but it is much weaker than the Somali jet. The three low-level jets over the South China Sea and the western Pacific (105°–110°E, 125°–130°E and 140°–145°E) exert more direct influences on the EASM system (Tao et al. 1962; Chen 1980; Wang and Tao 1984; Chen et al. 1991). Comparison between Fig. 8a and b shows that the LMD model simulates all the five low-level jets quite well. According to Wang and Tao (1984), strong episodes of these low-level cross-equatorial jets correspond to an intensification of the Australian Cold High and a more remarkable monsoon trough in the South China Sea.

As depicted in Fig. 8, there exist northerly flows in the upper troposphere during summertime. They are the return winds of the monsoon meridional cell. Notice that the northerly airflow at low level along 70°E in the model is the counterpart of the exaggerated anticyclone straddling the equator shown in Fig. 2b. Figure 9 displays a meridional and vertical cross section of the vertical wind. It is zonally averaged for the monsoon region (55–140°E). For both the observation and the

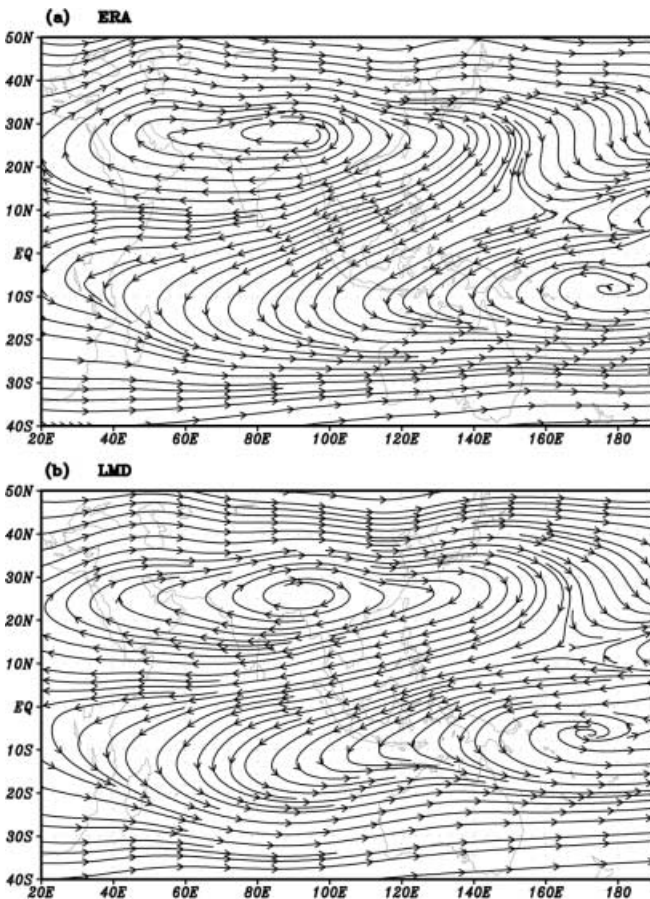


Fig. 6a, b. Same as in Fig. 2, but for 200 hPa

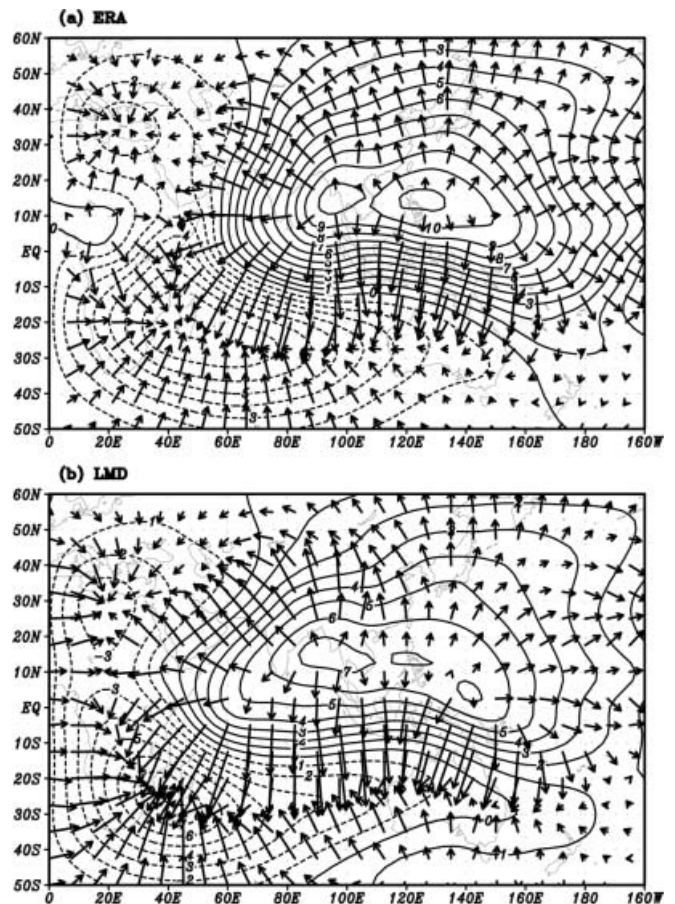


Fig. 7. JJA mean velocity potential at 200 hPa for the ECMWF reanalysis (a, ERA) and the model (b, LMD) respectively. Contour interval is $1 \times 10^6 \text{ m}^2 \text{ s}^{-1}$. Vectors indicate the divergent wind

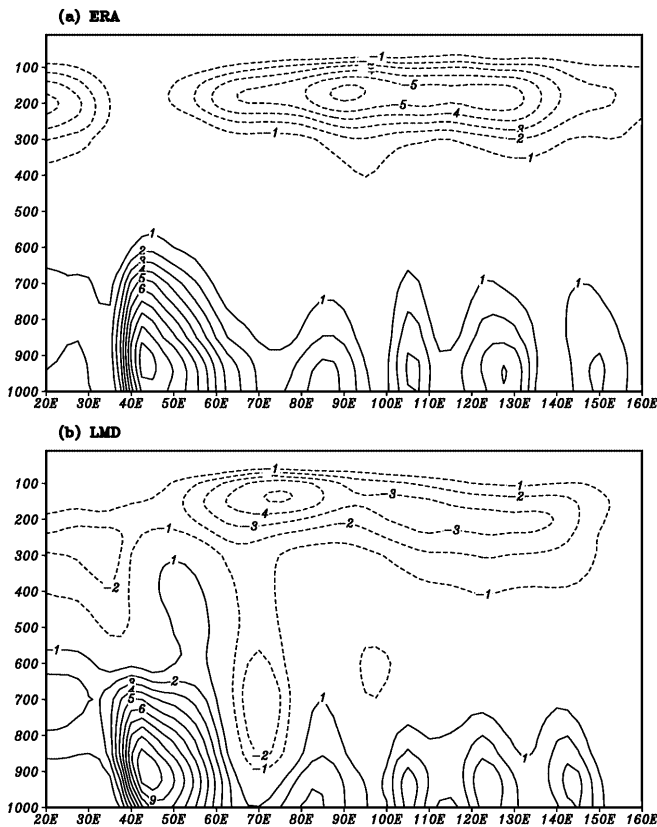


Fig. 8. JJA mean low-level jets depicted by the cross section of the meridional wind speed along the equator for the ECMWF reanalysis (a, ERA) and the model (b, LMD) respectively. Contour interval is 1 m s^{-1}

simulation, upward movement takes place from 5°S to 40°N and downward movement dominates 10°S to 40°S . Nevertheless, some discrepancies should be noted. In the observation, very strong rising movement is located between 15°N and 25°N . The model, however, gives a too weak movement there, indicating too weak convection and precipitation. The model's strongest center shifts southwards to the equator, where intense convection takes place.

By combining the meridional and vertical winds, we can draw a complete image of the meridional circulation. Figure 10 displays the JJA mean stream lines obtained from the ERA dataset and the simulation. The uppermost panel (Fig. 10a) shows the average for the monsoon region (from 55°E to 140°E) and the upper middle panel (Fig. 10b) depicts the average for the rest of the Earth's longitudes. The upper middle panel corresponds roughly to the normal image of Hadley cells in low latitudes and Ferrel cells in mid latitudes. For the monsoon region, strong upward motion shows at $20^{\circ}\text{--}30^{\circ}\text{N}$ of the Northern Hemisphere, and strong convergence dominates the region around 35°N . It is clear that the normal Hadley cell is replaced in this region by a meridional circulation of opposite sense which is often referred to as the monsoonal meridional cell (Chen et al. 1964; Ye and

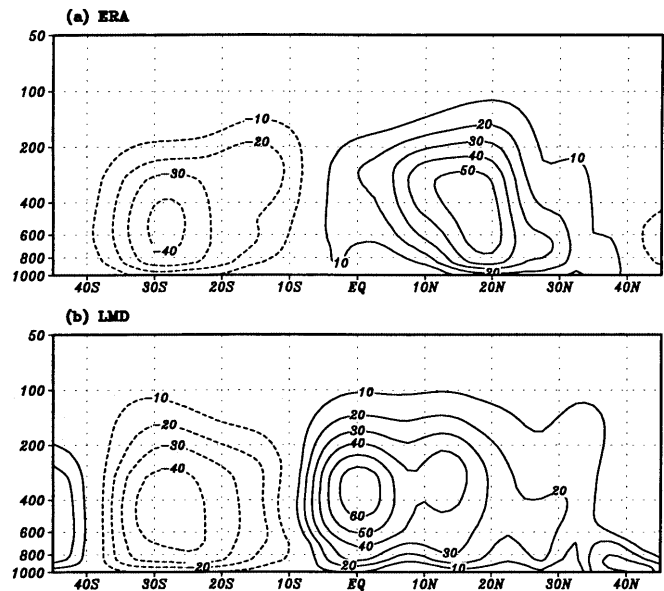


Fig. 9. JJA mean vertical velocity ($-10^{-3} \text{ hPa s}^{-1}$) averaged for the longitudinal range of $55\text{--}140^{\circ}\text{E}$ for the ECMWF reanalysis (a, ERA) and the model (b, LMD) respectively

Yang, 1979). Corresponding results of the model are displayed in Fig. 10c–d. The simulated monsoonal meridional cell is quite realistic, with ascending flows extending northwards up to 35°N and descending motions in the Southern Hemisphere.

The most pronounced difference of the meridional circulation between the Indian monsoon and the East Asian monsoon is that the highly elevated Tibetan Plateau inhibits the southward penetration of midlatitude flows to India in the low levels of the atmosphere. This determines the Indian monsoon to be purely a tropical monsoon. For eastern China, however, there are no high mountain barriers and the midlatitude flow can go straight into southern China and converge with the northward flows. This makes the EASM a mixture of tropical and subtropical monsoons. In comparing the meridional circulation along 80°E with that along 110°E , this difference is very obvious. The LMD model captures these features with high degrees of fidelity as shown in Fig. 11.

In general, the LMD model reproduces the EASM monsoonal meridional circulation successfully. Nevertheless, there still exists some difference between the simulation and the observation, for example, the observed relatively strong convergence at 35°N and its neighboring region (Fig. 10a) is weakly reproduced (Fig. 10c). The largest bias exists in the center of the vertical motion. As shown in Fig. 9a, the most vigorous motion revealed by the ERA data locates around 20°N , in the simulation (Fig. 9b), however, the subtropical vertical motion center shifts equatorwards, and there is another vigorous vertical motion centered around the equator that is absent from the observations. This is coincident with the weakly simulated divergent center at 200 hPa shown in Fig. 7b.

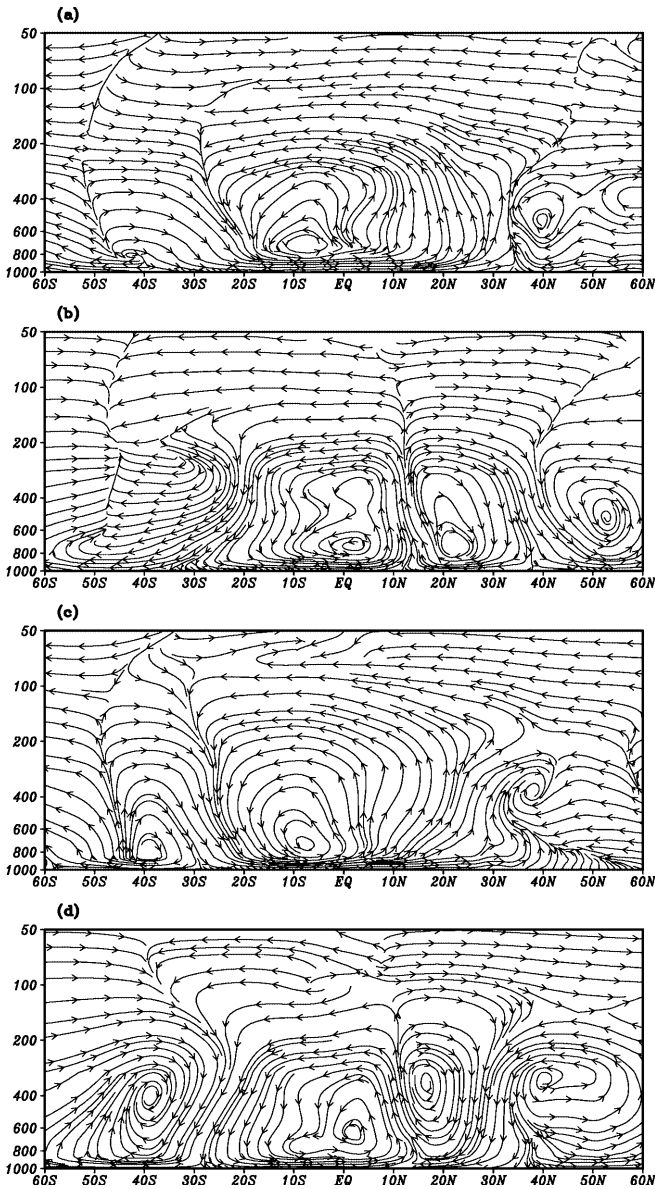


Fig. 10. JJA mean meridional circulations for **a, c** the longitudinal range of 55–140°E and **b, d** rest of the world. **a** and **b** are from the ECMWF reanalysis and **c** and **d** from the model

3.3 Humidity and precipitation

The moisture pattern is closely related to the monsoonal circulation and the associated moisture transport. Figure 12 shows the observed and simulated JJA mean specific humidity fields at 925 hPa. From observations, we can see clearly a high-humidity center in the northern portion of the Bay of Bengal which is associated with the intense Somali low-level jet. A second high-humidity center is near the Philippines and Taiwan, with an extension to the Yangtze River Valley (see the shaded region). This is related to the low-level jets on the southern and western flanks of the western Pacific subtropical anticyclone. The model simulates the first high-humidity center well, but the second one

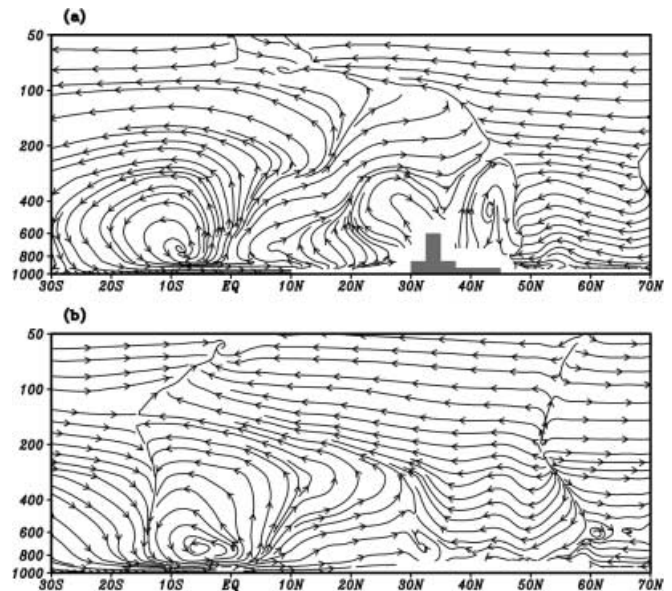


Fig. 11. The simulated JJA mean meridional circulation along **a** 80°E and **b** 110°E respectively

is missed. This is partly due to the discrepancies of the simulated subtropical anticyclone: too weak in central intensity but too strong in westward extension of its ridge tip. In the simulation, the airflow of the Indian summer monsoon does not extend far enough to the east, and it turns too early to the north after merging the trade wind in the southern flank of the western Pacific subtropical anticyclone. This is the reason why the simulated moisture distribution is too zonal in South and East China.

We present, in Fig. 13, the vertically integrated water vapor transport obtained from ERA, and the difference between ERA and the simulation. We can see that the contribution of the southwest monsoon to the water vapor transport over the EASM region is stronger in observation than in the model, i.e., the southwest monsoon flow in the LMD model has a smaller contribution to the moisture convergence over the EASM region. This deficiency is coincident with the simulated large-scale circulation discussed.

The bias in reproducing the moisture distribution and transport will ultimately affect the simulation of rainfall. Figure 14 shows the JJA mean precipitation fields of Xie and Arkin (1997) and the model respectively. The observed marked rainbelt stretches from the eastern Arabian Sea to the Bay of Bengal, and further to the western Pacific. This corresponds mainly to the airflow of Indian summer monsoon which begins from the East African coast and ends in the western Pacific. The rainfall pattern displays the typical feature of the summertime Intertropical Convergence Zone. We can find topography modulated strong rainfall in the western part of Indian Peninsula, western part of Indochina and western part of the Philippines. We can also see weak rainfall on the leeward of these landmas-

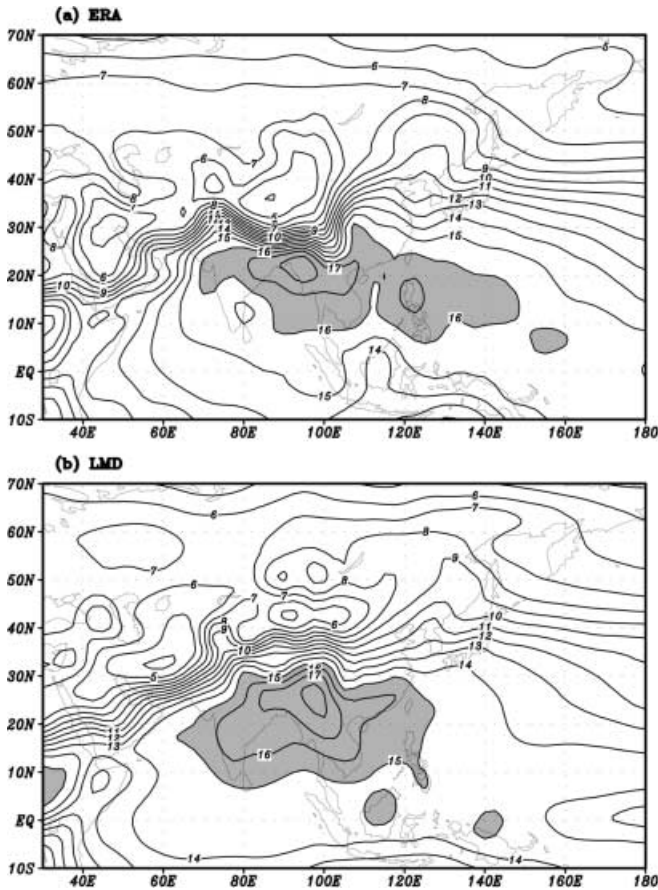


Fig. 12. JJA mean specific humidity (g kg^{-1}) at 925 hPa for the ECMWF reanalysis (a, ERA) and the model (b, LMD) respectively. The values over the Tibetan Plateau are extrapolated ones since 925 hPa locates under the ground surface

ses. The model does produce this clear rainbelt with correct topographical modulation, but there is a spurious marked band near the equator, from the west Indian Ocean to the western Pacific. This discrepancy is related to the too strong vertical ascending motion around the equator (see Fig. 9) and the distorted circulation patterns in the Indian Ocean, as revealed by the stream lines of 850 hPa (Fig. 2b) and the vertically integrated water vapor transport (Fig. 13b). The simulated rainfall centers in the western part of Indian Peninsula, and the western part of Indochina are also weaker than the observations. This feature is coherent with the deficiency in the vertically integrated water vapor transport shown in Fig. 13b.

For East Asia, abundant rainfall can be observed on the flank of the subtropical anticyclone, which is correctly simulated by the model. The observed marked rainbelt along the Yangtze River Valley (see the shaded rainbelt in Fig. 14a) is however missed in the simulation. This can be interpreted partly as the result of the weakly reproduced upward motion around 30°N as shown in Fig. 9. The observed monsoonal precipitation along the Yangtze River Valley is the product of the Meiyu front, which is quasi-stationary and is a characteristic feature

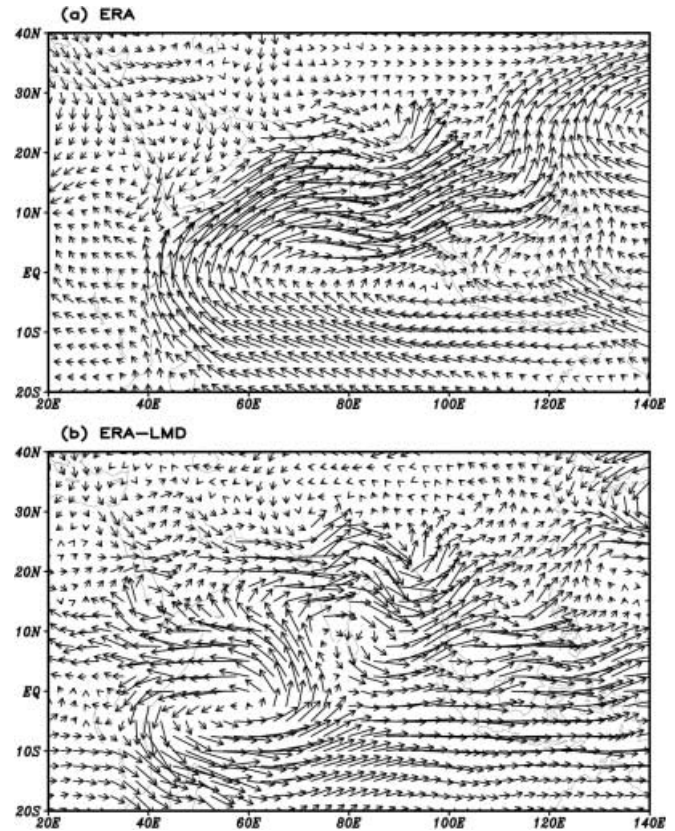


Fig. 13. JJA mean vertically integrated water vapor transport for the ECMWF reanalysis (a, ERA) and b the difference between ERA and LMD model

of the interaction between the warm/moist winds from the south and the cold/dry airflow originating from the north (Lau and Li 1984). In the mid-troposphere, the ridge of the western Pacific subtropical high usually determines the location where the warm air from the south meets the cold air from the north. The weakly reproduced subtropical high leads to a reduction of the subtropical southwest monsoon on its western flank, and then the convergence of the subtropical southwest monsoon with the mid-latitude westerly is weakened. This in turn causes the scarcity of rainfall over the Yangtze River Valley. In addition, the distorted cyclone over the Indian Peninsula (see Fig. 3) also results in a weak contribution of southwest monsoon to the moisture convergence over the Yangtze River Valley, which has been shown clearly in Fig. 13b.

From a large-scale perspective, as shown in Fig. 14, the precipitation distribution in continental China decreases from southeast toward northwest. This feature is related to the fact that when the monsoonal airflows move inland to the north and the west, they become drier and drier, producing less and less precipitation. The relatively successful reproduction of this feature is closely linked with the realistic model topography. On the southern and eastern flank of the Tibetan Plateau, the intense rainfall is due to the land-lifting effect. We can also notice the obvious rainfall centers in southeast

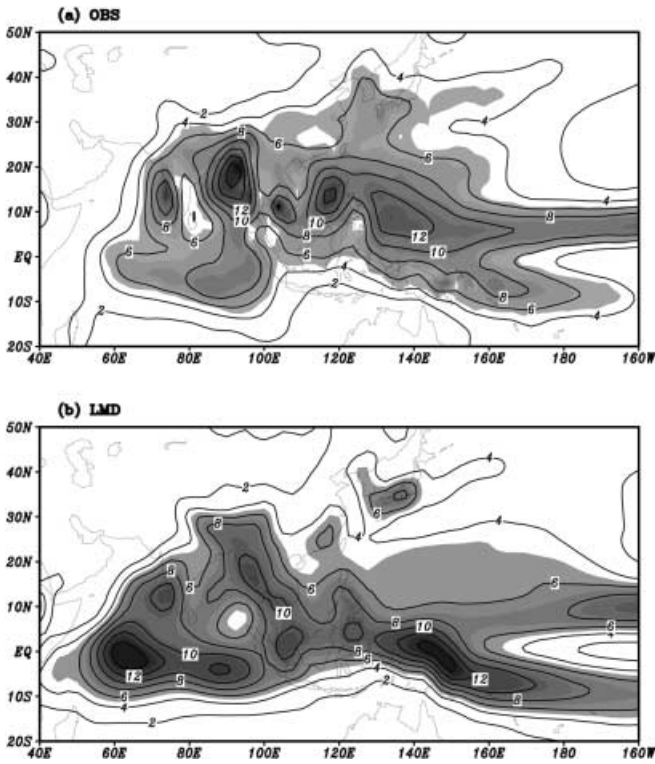


Fig. 14. JJA mean precipitation (mm day^{-1}) from **a** the observation of Xie and Arkin (1997) and **b** from the model. Contour interval is 2 mm day^{-1} . Shaded are regions greater than 5

and northeast China. Careful examination reveals that the model precipitation is locked into the topography much too closely. This is a common problem in many models.

4 Discussions

4.1 Role of plateau and tropical heating

The fundamental monsoonal feature is closely linked to the large land–sea thermal contrast (Murakami and Ding 1982). The key driving force for the summer monsoon is the available potential energy generated by the differential heating between land and sea (Zhang et al. 1997). The weakly simulated summer monsoon and the associated rainfall, including departures in planetary circulation such as the insufficient upper level return flow, are inherently related to the false position of the tropical convective heating and the relatively weaker plateau heating.

For the effect of tropical heating, the rainfall is an integrated measurement of the atmospheric latent heating. The observed rainfall has its most noted center over the northern portion of the Bay of Bengal, with two other centers over the South China Sea and western Pacific. This indicates strong heating and thus upper-atmosphere divergent centers over these regions (compare Figs. 7 and 14). For the simulation, however, although there exist rainfall centers around the Bay of

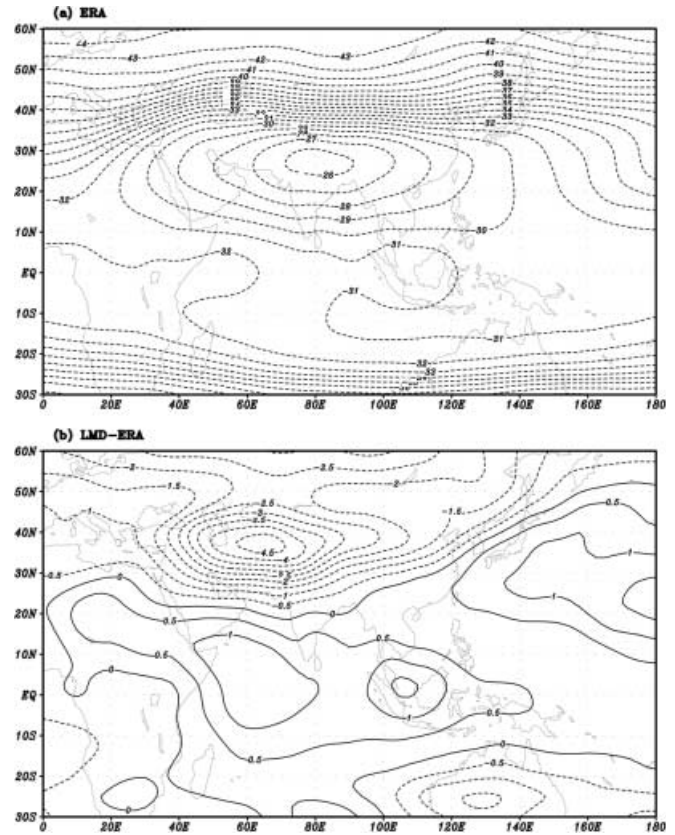


Fig. 15. JJA mean temperature averaged between 300 and 500 hPa for **a** ERA and **b** the difference between LMD and ERA. Contour interval is $1 \text{ }^{\circ}\text{C}$

Bengal and Philippines (with weaker intensities in comparison with the observations) associated with centers of 200 hPa velocity potential, two even clearer rainfall centers are found over the equatorial west Indian Ocean and Papua New Guinea, respectively. Since the mean position and intensity of tropical convection are closely related with the atmospheric general circulation (Branstator 1983), these spurious equatorial rainfall centers (and the associated latent heating) thus have negative effects on the simulated Indian monsoonal low and other large-scale circulation patterns.

Figure 15a displays the summertime tropospheric mean temperature (from 500 hPa to 300 hPa) obtained from ERA. There exists a planetary-scale warm air mass over South Asia with maxima over the southern Tibetan Plateau, resulting in strong temperature gradients in both the meridional and zonal directions. The upper tropospheric flow pattern shown in Fig. 6 clearly reflects this thermal contrast. Figure 15b shows the difference between the model and ERA. While the tropical tropospheric air and subtropical western Pacific air are slightly warmer ($0.5\text{--}1.5 \text{ }^{\circ}\text{C}$) than the observation, the air over the plateau is much colder in the model (about $4.5 \text{ }^{\circ}\text{C}$ in the center). This bias greatly reduces the land–sea thermal contrast in both meridional and zonal directions, and thus the monsoon intensity.

Careful examination reveals that the weak plateau heating in the model results mainly from the excessive low-level cloud, which considerably reduces the incoming solar radiation. Figure 16 shows the difference between the LMD model and the ERA dataset for respectively low-level cloud cover, net surface solar radiation and surface temperature. Regions covered by excessive (insufficient) low-level cloud coincide well with regions of insufficient (excessive) solar radiation and colder (warmer) surface temperature. Codron (2001) suggested that this is related to an inadequate treatment of moisture advection in a large and steep mountain region.

4.2 Effects of local zoom

The comparisons made show that the variable resolution LMD model performs well in reproducing the EASM system, although some deficiencies exist concerning the moisture and precipitation. How much of the merits (or discrepancies) of the model are associated with the employment of local zoom technique? To assess this we performed another simulation without using the local zoom (following the same procedure and the same duration as described in Sect. 2). The spatial resolution in this second simulation is globally homogenous: $3^\circ \times 2^\circ$ in longitude and latitude. It should be pointed out that no other difference exists between the two integrations except the horizontal grid distribution.

Figure 17 shows the JJA mean 500 hPa geopotential height and the cross-equator low-level jets as produced by the model without local zoom. The intensity of the subtropical high is weaker in comparison with that shown in Fig. 5b. For instance, the central intensity of the high shown in Fig. 5b has a value of 5870 gpm, the corresponding intensity of Fig. 17a is about 10 m weaker, i.e., 5860 gpm. Thus the employment of local zoom over the EASM region definitely results in a better reproduction of the western Pacific subtropical high. Similar improvements can be found in the simulation of the low level jets across the equator. The cross-equator low-level jets situated between 100°E and 130°E in Fig. 17b are inferior to those shown in Fig. 8b.

We also used some quantitative measurements to evaluate the difference between the two configurations of the model. Following Walsh and McGregor (1995), the pattern correlation coefficient and the rms (root-mean-square) error can be used to quantify the quality of the two simulations. The reference state is from ERA dataset. Both ERA and the LMD simulations are interpolated into a $2.5^\circ \times 2.5^\circ$ grid before performing the calculation. The geographic domain covers the extended EASM region ($0^\circ\text{--}180^\circ\text{E}$, $30^\circ\text{S}\text{--}60^\circ\text{N}$).

Table 1 shows pattern correlations and rms errors for JJA mean geopotential height and temperature of 500 hPa. For both the geopotential height and the temperature, the pattern correlations of the model employing local zoom are higher than that employing regular mesh, while the rms errors are reduced. Thus, the

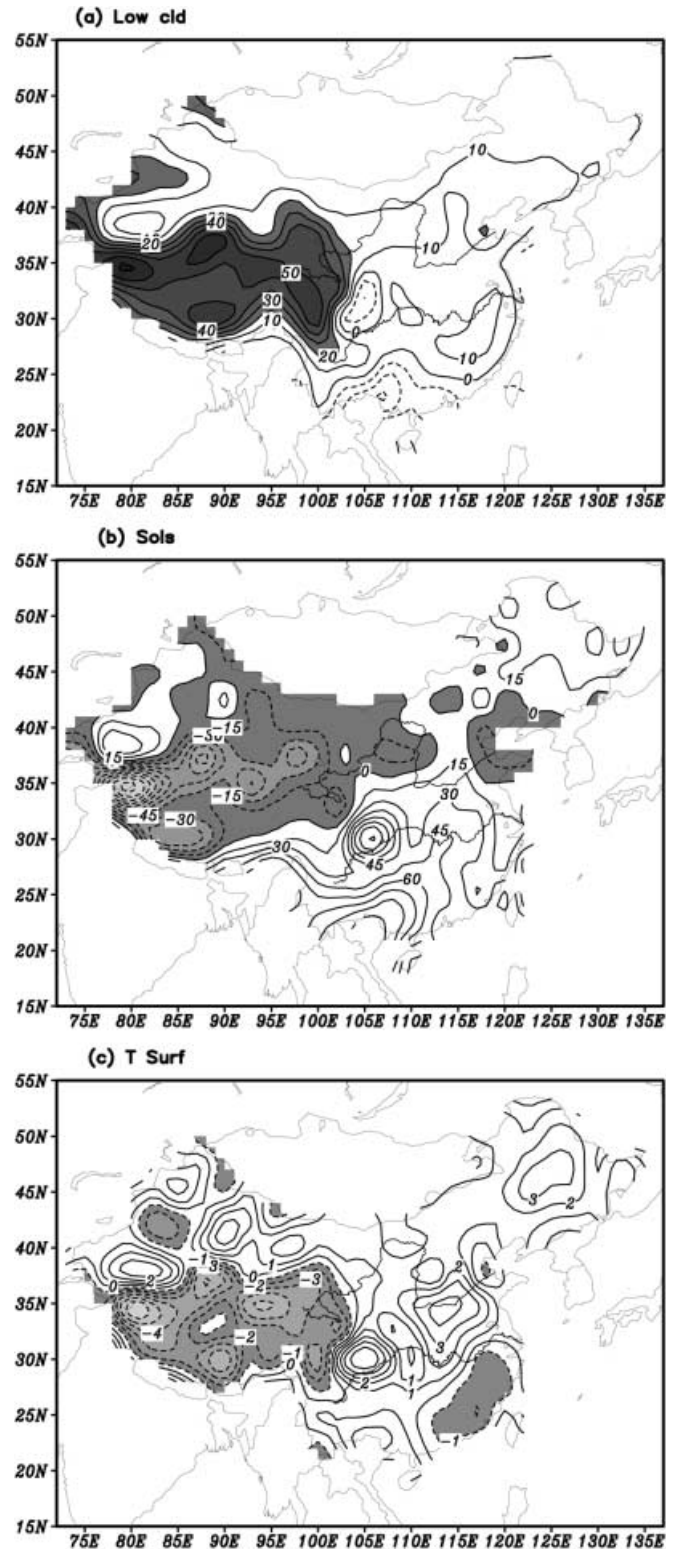


Fig. 16. Difference between LMD and ERA for JJA-mean **a** low-level cloud, **b** net surface solar radiation (W m^{-2}) and **c** surface temperature ($^\circ\text{C}$)

performance of the model employing local zoom is definitely superior to that employing regular coarse mesh in this regard.

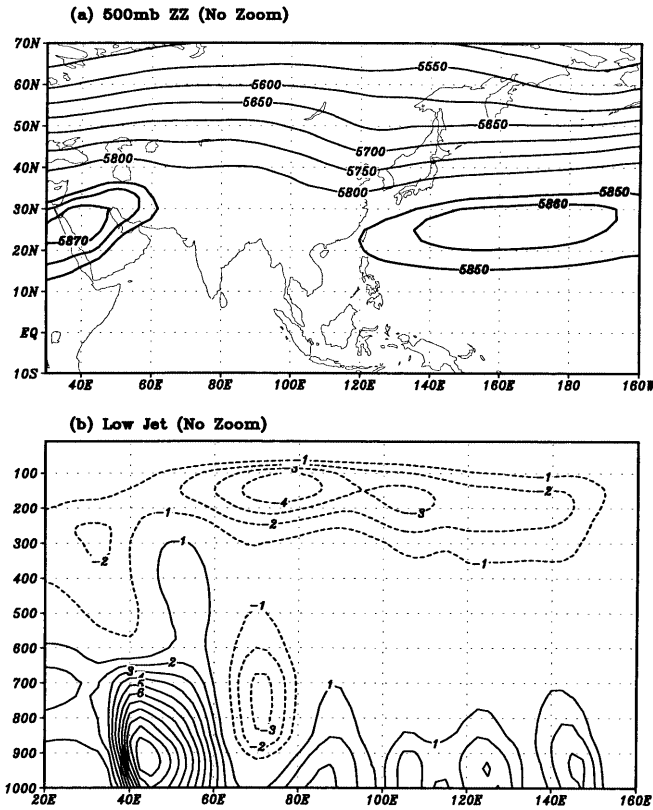


Fig. 17. a JJA mean 500-hPa geopotential height and b the cross-equator low level jets simulated by the LMD model without local zoom

It should be noted that while statistical measures and qualitative comparisons reveal some improvements resulting from local zoom procedure no evidence, from visual inspection, has been found in the distorted low pressure trough over the Indian subcontinent. There the simulation with local zoom is nearly the same as the simulation without it in this case. This is also so for the insufficient plateau heating, the 200 hPa divergence and the precipitation, indicating that these deficiencies of the LMD model are inherent to the model’s physical parametrization and cannot be overcome by simply using the local zoom technique.

In a general manner, the improvement of the EASM simulation obtained by the local zoom is not as pronounced as expected. The reason is that the regular-grid simulation is already at high resolution ($3^{\circ} \times 2^{\circ}$) and the

difference in resolution for the two simulations is not large enough (a factor of 2 near the center of the zoom). Regional model studies show that a horizontal gridpoint spacing of 50–60 km over the EASM domain is probably necessary to offer a relatively successful simulation (Wang et al. 2000; Liu et al. 1994). This suggests that the local zoom technique with larger enlargement factor over the EASM region should be investigated in the future.

5 Concluding remarks

The performance of LMDZ, a variable-resolution atmospheric GCM, in reproducing the EASM has been evaluated through the comparison of the model output against the observation. This high local-resolution model, with its realistic surface topography representation, is able to capture the main features of the EASM. Encouraging results have been found in the simulation of the large-scale monsoon airflows, the monsoon trough in the South China Sea, the cross-equatorial airflow, the monsoonal meridional cell, the upper-level divergent centers, the surface cold high in Australia, and the upper-level northeasterly return flow. For the subtropical anticyclone over the western Pacific, however, the simulation is weak in central intensity but extends too far westwards.

The model’s main deficiency lies in the simulation of monsoonal precipitation. While the local zoom centered on China leads to a well prescribed model terrain of the monsoon region that assures a satisfactory simulation of continental-scale summer rainfall, the observed heavy rainbelt along the Yangtze River Valley is missed in the model. This discrepancy is related to the improperly simulated western Pacific subtropical high. The strong rainbelt along the Yangtze River Valley is, in fact, the result of convergence of the cold and dry mid-latitude air with the warm and moist tropical and subtropical air. Analysis of the monsoonal meridional circulation shows that the convergence of cold and warm airflows around 35°N is realistically simulated in the model, but the intensity is too weak. The weakly reproduced subtropical high leads to a weaker subtropical southwest monsoon on its western flank. Furthermore, the excessive westward extension of the high prohibits the northeastward penetration of the tropical Indian monsoon, and thus inhibits the contribution of tropical warm and moist airflow to the convergence over the Yangtze River Valley. In addition, the distorted Indian low also weakens the contribution of the tropical southwest monsoon to the moisture transport over the EASM region.

The distinct monsoonal feature is closely related to the land-sea thermal contrast. While the summertime plateau heating is weaker in the model than in the observations, the simulated tropical latent-heat release is however slightly stronger. This results in a weak land-sea thermal contrast in both meridional and zonal directions. The weakly reproduced EASM precipitation including

Table 1. Pattern correlations (ρ) and root-mean-square (rms) errors between the simulations (with and without local zoom) and the observation, calculated for 500-hPa geopotential height (Z) and temperature (T) over the region 0° – 180°E and 30°S – 60°N

	500-hPa Z		500-hPa T	
	ρ (%)	rms (m)	ρ (%)	rms (K)
no zoom	97.8	16.7	97.5	1.1
zoom	98.0	16.4	98.0	0.9

the improperly simulated large-scale circulation such as the weaker upper level divergence is the consequence of this insufficient land-sea thermal contrast. Further analysis reveals that the weak plateau heating results from the excessive low-level cloud in the model.

The performance and problems of the LMD model revealed in the present study should be evaluated again when the physical parametrization of the model is changed. Future model development should be pursued in two aspects. One is towards parametrization of the atmospheric boundary-layer and associated low-level cloudiness. Another is towards the convection scheme or the current closure conditions in the Tiedtke scheme. Incorporation of other more performant convection schemes in the LMD model is also in progress.

Comparison with the simulation employing regular coarser mesh model reveals that the local zoom technique improves, in a general manner, the EASM simulation. The fact that the improvement is not as pronounced as expected suggests that a local zoom with an even larger expansion factor over the EASM region is needed. However, the employment of local zoom techniques can also introduce unrealistic short-wave noise in the regions of steep orographic gradient (for example, between the Tibetan Plateau and the Sichuan basin situated on the eastern periphery). This issue will be addressed in the future.

Acknowledgements The authors would like to thank R.-C. Yu and Y.-F. Guo for very helpful discussions and two anonymous reviewers for constructive comments on the manuscript. This work is a contribution to the Sino-France Advanced Science and Technology Cooperative Research Programme (PRA T99-03) and is partly funded by the European Commission through the SINTEX project and the Chinese Academy of Sciences under grant "Hundred Talents" for "Validation of Coupled Climate models".

References

- Branstator G (1983) Horizontal energy propagation in a barotropic atmosphere with meridional and zonal structure. *J Atmos Sci* 40: 1689–1708
- Chen YS (1980) The spectrum analysis of the cross-equatorial flow in the West Pacific in summer. *Sci Atmos Sinica* 4: 363–368
- Chen LX, Zhu QG, Luo HB, He JH, Dong M, Feng ZQ (1991) Eastern Asian Monsoon. Meteorology Press, Beijing, pp 292
- Chen QS, Li WL, Mao JH (1964) The mean flow fields and meridional cells in the regions of southwesterly monsoon over Southeast Asia and trade wind over the Pacific. *Acta Meteorol Sinica* 34: 51–61
- Codron F (2001) Sensitivity of the tropical Pacific to a change of orbital forcing in two versions of a coupled GCM. *Clim Dyn* 17: 187–203
- Deque M, Piedelievre JP (1995) High resolution climate simulation over Europe. *Clim Dyn* 11: 321–340
- Ding YH (1994) Monsoons over China. Kluwer, Netherlands, pp 1–90
- Gibson J, Kallberg P, Uppala S, Hernandez A, Nomura A, Serrano E (1997) ERA description. ECMWF Reanalysis Project Rep Ser 1, European Centre for Medium Range Weather Forecast, Reading, UK, pp 60
- Gong W, Wang WC (2000) A regional model simulation of the 1991 severe precipitation event over the Yangtze-Huai river Valley: Part II: model bias. *J Clim* 13: 93–108
- Krishnamurti TN, Bhalme HN (1976) Oscillation of a monsoon system. Part I: Observational aspects. *J Atmos Sci* 33: 1937–1954
- Krinner G, Genthon C, Li ZX, Le Van P (1997) Studies of the Antarctic climate with a stretched-grid general circulation model. *J Geophys Res* 102 (D12): 13,731–13,745
- Latif M, Sterl A, Assenbaum M, Junge MM, Maier-Reimer E (1994) Climate variability in a coupled GCM Part II: the Indian monsoon. *J Clim* 7: 1449–1462
- Lau KM, Yang S (1996) Seasonal variation, abrupt transition, and intraseasonal variability associated with the Asian summer monsoon in the GLA GCM. *J Clim* 9: 965–985
- Lau KM, Li MT (1984) The monsoon over East Asia and its global association – A survey. *Bull Am Meteorol Soc* 65: 116–125
- Laval K, Raghava R, Polcher J, Sadourny R, Forichon M (1996) Simulations of the 1987 and 1988 Indian monsoons using the LMD GCM. *J Clim* 9: 3357–3371
- Le Treut H, Li ZX (1991) Sensitivity of an atmospheric general circulation model to prescribed SST changes: feedback effects associated with the simulation of cloud optical properties. *Clim Dyn* 5: 175–187
- Li CF, Yanai M (1996) The onset and interannual variability of the Asian summer monsoon in relation to land-sea thermal contrast. *J Clim* 9: 358–375
- Li XZ (1956) A synthetic theory of formation of typhoons. *Acta Meteorol Sinica* 27: 87–100
- Li ZX (1999) Ensemble atmospheric GCM simulation of climate interannual variability from 1979 to 1994. *J Clim* 12: 986–1001
- Liang XZ, Wang WC (1998) Association between China monsoon rainfall and tropospheric jets. *Q J R Meteorol Soc London* 124: 2597–2623
- Liu YQ, Giorgi F, Washington W (1994) Simulation of summer monsoon climate over East Asia with an NCAR regional climate model. *J Clim* 122: 2331–2348
- Liu YQ, Avissar R, Giorgi F (1996) Simulation with the regional climate model RegCM2 of extremely anomalous precipitation during the 1991 East Asian flood: an evaluation study. *J Geophys Res* 101: 26,199–26,216
- Menendez CG, Saulo AC, Li ZX (2001) Simulation of South American wintertime climate with a nesting system. *Clim Dyn* 17: 219–237
- Murakami T, Ding YH (1982) Wind and temperature changes over Eurasia during the early summer of 1979. *J Meteorol Soc Japan* 60: 183–196
- Sadourny R, Laval K (1984) January and July performance of the LMD general circulation model. In: Berger A, Nicolis C (eds) *New Perspectives in Climate Modelling*. Elsevier, Amsterdam, pp 173–198
- Samel AN, Wang SW, Wang WC (1995) A comparison between observed and GCM-simulated summer monsoon characteristics over China. *J Clim* 8: 1690–1696
- Sharma OP, Le Treut H, Seze G, Fairhead L, Sadourny R (1998) Interannual variations of summer monsoons: sensitivity to cloud radiative forcing. *J Clim* 11: 1883–1905
- Shukla J, Fennessy MJ (1992) Some idealized experiments to diagnose the simulated Asian summer monsoon variability. WCRP-68, WMO/TD-No.470, Geneva, Switzerland, pp 2153–2157
- Slingo JM (1987) The development and verification of a cloud prediction scheme for the ECMWF model. *Q J R Meteorol Soc London* 113: 899–927
- Sperber KR, Hameed S, Potter GL, Boyle JS (1994) Simulation of the northern summer monsoon in the ECMWF Model: sensitivity to horizontal resolution. *Mon Weather Rev* 122: 2461–2481
- Tao SY, Chen LX (1987) A review of recent research on the East Asian summer monsoon in China: In: Chang CP, Krishnamurti TN (eds) *Review of monsoon meteorology*. Oxford University Press, Oxford, UK, pp 353
- Tao SY, Xu SY, Guo QY (1962) The circulation with the persistent flood or drought in the Yangtze River Valley in summer. *Acta Meteor Sinica* 32: 91–103

- Tiedtke M (1989) A comprehensive mass flux scheme for cumulus parameterization in large scale models. *Mon Weather Rev* 117: 1779–1800
- Vernekar AD, Ji Y (1999) Simulation of the onset and intraseasonal variability of two contrasting summer monsoons. *J Clim* 12: 1707–1725
- Walsh K, McGregor J (1995) January and July climate simulations over the Australian region using a limited-area model. *J Clim* 8: 2387–2403
- Wang JZ, Leftwich PW (1984) A major low-level cross-equatorial current at 110°E during the northern summer and its relation to typhoon activities. *Sci Atmos Sinica* 8: 443–449
- Wang SD, Tao SY (1984) The structure of the cross-equatorial flow in the South China Sea. *Acta Ocean Sinica* 6: 160–173
- Wang WC, Gong W, Wei HL (2000) A regional model simulation of the 1991 severe precipitation event over the Yangtze-Huai River Valley: Part I: precipitation and circulation statistics. *J Clim* 13: 74–92
- Webster PJ, Yang S (1992) Monsoon and ENSO: Selectively interactive systems. *Q J R Meteorol Soc London* 118: 160–173
- Webster PJ, Magaña VO, Palmer TN, Shukla J, Tomas RA, Yanai M, Yasunari T (1998) Monsoons: processes, predictability, and the prospects for prediction. *J Geophys Res* 103(C7): 14,451–14,510
- Xie PP, Arkin PA (1997) Global precipitation: a 17-year monthly analysis based on gauge observations, satellite estimates and numerical model outputs. *Bull Ame Meteorol Soc* 78: 2539–2558
- Ye DZ, Yang G (1979) Mean meridional circulations over East Asia and the Pacific Ocean. I: summer; II: winter. *Sci Atmos Sinica* 3: 299–305
- Yu RC, Li W, Zhang XH, Yu YQ, Liu HL, Zhou TJ (2000) Climatic features related to eastern China summer rainfalls in the NCAR CCM3. *Adv Atmos Sci* 17: 503–518
- Zeng QC, Liang XZ, Zhang MH (1988) Simulation on the abrupt change of monsoon and the general circulation. *Sci Atmos Sinica* (special issue) 22–42
- Zhang Y, Sperber KR, Boyle JS, Dix M, Ferranti L, Kitoh A, Lau KM, Miyakoda K, Randall D, Takacs L, Wetherald R (1997) East Asian winter monsoon: results from eight AMIP models. *Clim Dyn* 13: 797–820